

A posteriori insertion of information for focusing and time–depth conversion of ground-penetrating radar data

Raffaele Persico¹  | Francesco Marasco¹ | Gianfranco Morelli² | Giuseppe Esposito³ | Ilaria Catapano³

¹Department of Environmental Engineering, University of Calabria, Rende, Italy

²Geostudi Astier srl, Livorno, Italy

³Institute for the Remote Sensing of the Environment IREA-CNR, Naples, Italy

Correspondence

Raffaele Persico, Department of Environmental Engineering, University of Calabria, Rende, Italy.
 Email: raffaele.persico@unical.it

Abstract

This paper deals with ground-penetrating radar prospecting and exploits a semi-heuristic strategy to account for inhomogeneous background media, empty cavities or topography of the surface. We assume here that no more than a commercial processing software is available. Customarily, commercial codes assume a homogeneous soil and a flat interface in order to achieve the focusing of the data. Therefore, this is also the model exploited here, whereas the data are referred to an inhomogeneous soil or to a non-flat interface. The proposed strategy exploits the principle that ‘the data speak’, even if with some ambiguity and some reticence, and they can reveal or at least suggest important features of the underground scenario. On this basis, heuristically, we exploit features derived from the data themselves as a posteriori information, improving the available focusing and time–depth conversion even having at disposal a basic model of the background scenario.

KEYWORDS

ground-penetrating radar, imaging, interpretation, migration

INTRODUCTION

Ground-penetrating radar (GPR) prospecting allows the characterization of a large variety of subsurface scenarios. However, the reliability and accuracy of the results depend on the adopted data processing chain and, often, on the validity of the a priori assumptions underlining it. Specifically, the commercial GPR data processing tools available for users customarily make simplifying hypotheses on the scenario under test, which do not correspond to the real situation, and this can lead to unsatisfactory results. A typical example is the soil representation, being the soil usually modelled as a homogeneous medium with a flat air–soil interface, even if this is not always true. In this frame, it is worth remarking that, if the soil is homogeneous and the air–soil interface is flat, the exact value of propagation velocity of the medium is also

the value that guarantees the correct time–depth conversion and that provides the best focusing of buried anomalies when inserted in a migration (Schneider, 1978; Stolt, 1978; Webster et al., 2019) or an inverse scattering (Catapano et al., 2019; Colica et al., 2021; Webster et al., 2019) algorithm. Conversely, outside this canonical situation, the focusing step can get more complicated if the user does not have the possibility to model properly the reference scenario at hand. Accordingly, imaging approaches based on properly defined scattering models have been proposed. In particular, in Gennarelli et al. (2021), the authors deal with a linear microwave tomographic approach allowing accurate imaging results in presence of a heterogeneous background soil, whose dielectric permittivity changes along depth, while keeping the computational complexity of the same order of that experienced for canonical homogeneous scenarios. In Lambot and André (2014), the

This is an open access article under the terms of the Creative Commons Attribution-NonCommercial License, which permits use, distribution and reproduction in any medium, provided the original work is properly cited and is not used for commercial purposes.

© 2023 The Authors. *Geophysical Prospecting* published by John Wiley & Sons Ltd on behalf of European Association of Geoscientists & Engineers.

reconstruction of the stratification of a soil made by a multi-layered medium (with layers parallel to the air soil interface) is faced, but under the hypothesis that the layers are flat and parallel to the air–soil interface. It is also possible to make use of reverse time migration (TRM) algorithms (Alani et al., 2020; Feng et al., 2022; Mao et al., 2021; Wang et al., 2019) that can account for the inhomogeneity of the background medium. However, they are in general associated to a forward solver, which could be unavailable or might be not user friendly, especially in complex scenarios. Moreover, as outlined in Mao et al. (2021), sharp discontinuities can cause low frequency noise on TRM algorithms, whereas, as outlined in Feng et al. (2022), a good knowledge of the inhomogeneous background medium is needed in order to achieve reliable results from TRM, which might be unavailable. Further methods are the distorted Born inverse scattering algorithm based on a numerical evaluation of the Green's function (Chew, 1995) and iterative approaches based on conjugate gradient based minimizations of the relevant cost functional (Moghadam et al., 2005; Ye & Chen, 2017). All these approaches are based on models more refined than a standard migration algorithm (Schneider, 1978; Stolt, 1978) that customarily are not available in commercial codes for GPR data processing.

This paper assumes that just a standard migration algorithm, suited for a homogeneous soil and a flat interface, is available for the data processing and proposes a heuristic strategy capable to face some more complex scenarios mitigating the problems related to this complexity.

The proposed strategy is not mathematically rigorous but it is able to improve the visualization of the targets of interest in applicative cases and in absence of processing codes based on complex scattering models. This is of interest in common praxis, because rarely complex models are commercially available and user friendly enough to be exploited outside research contexts.

In particular, the strategy combines migration results according to the observation of separately achieved reconstructions. Therefore, it makes the use of information heuristically deduced a posteriori, that is after a first basic solution of the problem. This strategy was already applied on real data gathered in the field (Persico & Morelli, 2020, 2021), and it provided fully reasonable results, even if no excavation was possible at the moment.

In the following, we consider four examples regarding the following scenarios:

1. A two-layered soil with the lower medium emerging somewhere up to the air soil interface.
2. A two-layered soil with the lower medium covered everywhere by the upper one.
3. A soil with buried empty cavities.
4. A soil characterized by a meaningful topography of the air soil interface.

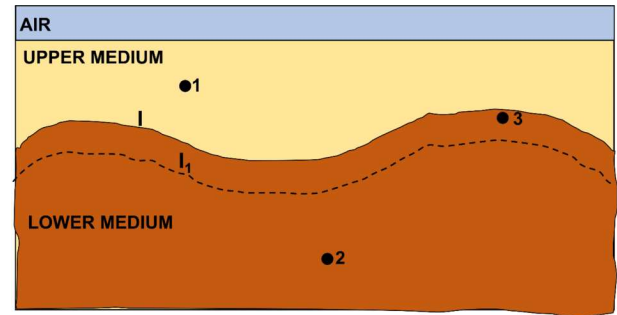


FIGURE 1 Schematic of three targets in a two-layered medium.

The common aspect of these four cases is that, making use of a standard migration algorithm, the actual wave propagation velocity in the soil is not the value that guarantees the best focusing of all the targets. Another common aspect, related to the previous one, is that the diffraction curves (that in these cases are not necessarily hyperbolas; Persico et al., 2015) do not provide necessarily a correct evaluation of the propagation velocity.

The paper structure is as follow. ‘Combined migration and combined time–depth conversion’ section briefly explains the concepts of the combined migration and time–depth conversion. This is proposed for the sake of self-consistency, but for more details, the interested reader is referred to Persico and Morelli (2020,2021). Then, the above listed scenarios will be sequentially considered. An experimental result is then shown too in ‘Experimental results’ section. Conclusions will follow.

COMBINED MIGRATION AND COMBINED TIME–DEPTH CONVERSION

Let us consider the layered scenario sketched in Figure 1. From the surface, we can evaluate the propagation velocity in the upper medium but not in the lower medium; at least, we cannot evaluate it with a conventional ground-penetrating radar (GPR) system working in common offset mode (Webster et al., 2019). With regard to Figure 1, the retrieved value of the propagation velocity in the upper medium is also the most suitable velocity value to focalize target 1. However, being the soil not homogeneous, the best velocity value to focalize target 2 and target 3 is neither the propagation velocity in the upper medium nor that in the lower medium. Notwithstanding, some intermediate value between the wave velocities in the upper and lower medium will be presumably (and heuristically) the best one in order to provide a good focusing of target 2 and target 3 with a basic migration algorithm. This intermediate value depends on the target position, and therefore, the value optimal for some target might be not optimal for some other target. Notwithstanding, a reasonable averaged choice is presumably achievable in

many cases. In particular, for target 3, which represents an object located in the lower medium but close the upper medium, probably the propagation velocity of the upper medium will allow a good focalization, because the waves impinging on it and scattered from it to the receiving antenna mainly propagate in the shallower layer. Therefore, in order to focalize target 1 and target 3, a reasonable heuristic choice is to perform the migration by using the propagation velocity value of the upper medium. Conversely, we expect to achieve the best focusing of target 2 by using a wave propagation velocity intermediate between that of the upper and lower medium. Such a value is not easy to be predicted but can be heuristically determined by means of a trial procedure.

According to the above observations, in order to implement a combined migration, we apply the standard migration approach twice: first, by using the propagation velocity of the upper medium (as retrieved e.g. by means of the diffraction hyperbolas in the upper medium); second by using the heuristically determined propagation velocity value optimizing the focusing of the target into the deeper layer. Then, we combine the two results in order to compose a reasonable focusing of all the targets of interest. It is worth pointing out that, usually, the curved line at which one should join the two migration results is not necessary the actual interface between the upper and lower media but rather a deeper line curve approximately parallel to the interface between the two soil layers. In Figure 1, this curve is schematized by means of the dashed line I_1 , being I the physical interface between the two layers. The definition of the line I_1 is heuristic too (Persico & Morelli, 2021). The combined migration essentially performs the joining of two different migration results, seamed together along the line I_1 . Of course, the part of the image higher than this line is taken from the migration result that best focuses the targets shallower than I_1 , whereas the other piece is taken from the migration results that best focus the targets deeper than I_1 . However, a mere joining of these two pieces would result into a visible seam effect in correspondence of I_1 . Therefore, a linear vertical transition along a belt centred on I_1 is introduced too, which erases this effect (Persico & Morelli, 2020, 2021).

The proposed combination of migrated results makes more sense if we apply also a combined time–depth conversion, that is a time–depth conversion that accounts for the different velocities in the two layers. In order to do this, first, we have to evaluate the propagation velocity in the lower medium. In fact, the propagation velocity of the lower medium previously exploited for the combined migration is not the actual one due to the inhomogeneity of the soil, as explained before. In the lack of a refined model for the wave propagation, the propagation velocity in the second medium cannot be evaluated from GPR data. However, its value can be deduced from some localized ground truthing (Conyers & Goodman, 1997) or from time domain reflectometry measurements (Cataldo et al., 2011). Once the velocity in the second layer has been

fixed, we have to evaluate the maximum spatial depth reached in the spatial domain within the investigated domain. In fact, data gathered in time domain are referred to a unique time bottom scale for any position of the antennas, and therefore, (as the interface I is not flat) the maximum imaged depth level is variable versus the abscissa. The maximum depth versus the abscissa is easily evaluated as the spatial depth corresponding to the abscissa at which the faster layer achieves its maximum thickness in time domain. This maximum depth will be the spatial bottom scale in the time–depth converted image.

However, it is not sufficient to determine the spatial bottom scale. To highlight this aspect, let us label the time step as Δt . This time step is the same for both layers; however, the corresponding vertical spatial step is not. In particular, let us label as v_1 and v_2 the propagation velocity in the upper and in the lower layer, respectively. We have two native vertical spatial steps given by

$$\begin{cases} \Delta z_1 = \frac{v_1 \Delta t}{2} \\ \Delta z_2 = \frac{v_2 \Delta t}{2} \end{cases}, \quad (1)$$

for the upper and the lower layers, respectively. If we label as Δz the minimum between these two values, then both the upper and lower medium should be sampled with this spatial step. In fact, if we do not perform this resampling, we reproduce the exact comprehensive depth of the investigated zone, but the targets in the medium with lower propagation velocity will appear expanded, whereas those in the layer with higher propagation velocity will appear compressed. Moreover, the barycentre of all the targets (both in the upper and in the lower layer) will be shifted towards the air–soil interface if the wave propagation velocity in the shallower layer is the higher one, otherwise they will be all imaged deeper than their actual depth if the waves are faster in the deeper layer. Of course, also the interface between the layers will be not correctly converted from time to depth with a simple imposition of the maximum spatial depth.

To report both layers to their correct spatial step means to resample the part of the result related to the faster propagation velocity with a depth step Δz . This resampling has to be performed column per column, because the vertical extension of the faster layer depends on the abscissa, due to the curvature of the line I that separates the two layers. Still more in detail, the resampling amounts to resample the faster part of each column of the combined matrix along $N_j = \frac{Z_j}{\Delta z}$ samples, where Z_j is the comprehensive spatial thickness of the faster medium at the current abscissa (which is accounted by the value j of the column index). In its turn, the local thickness Z_j of the faster medium is calculated as $Z_j = \frac{\max(v_1, v_2) N_{1j} \Delta t}{2}$, where N_{1j} is the original number of cells relative to the faster medium at the current abscissa, and the quantity $N_{1j} \Delta t$

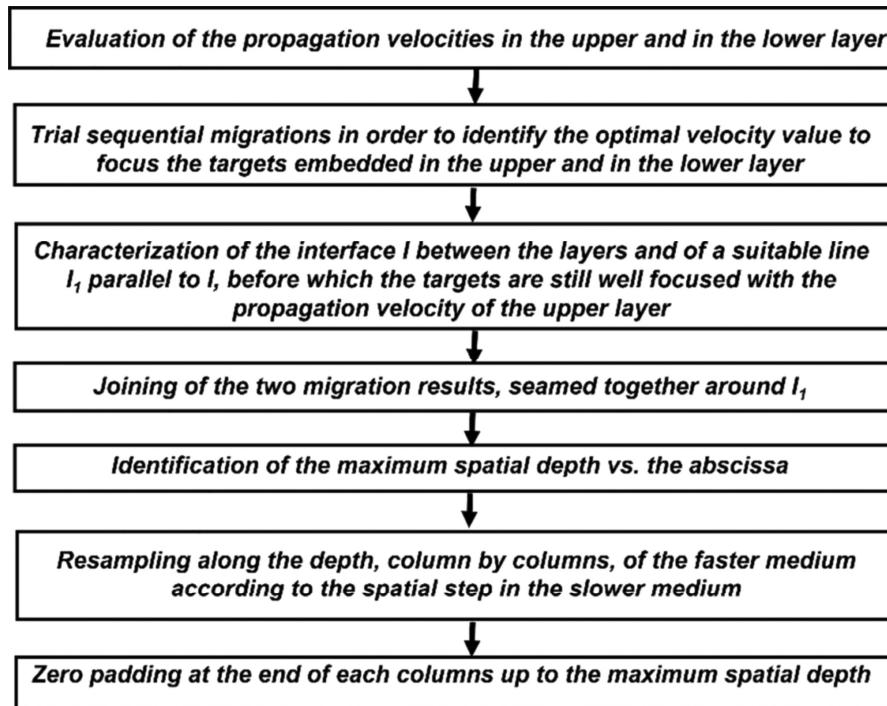


FIGURE 2 Flow diagram of the operations needed for a combined migration and a combined time–depth conversion in a two-layered medium.

represents the time thickness of the faster medium at the current abscissa. Of course, the ratio $\frac{Z_j}{\Delta z}$ is not always an integer quantity, and thus, the integer number closest to this ratio is taken. It is an elementary calculation to work out that in the end, we have $N_j = N_{1j} \frac{\max(v_1, v_2)}{\min(v_1, v_2)}$, that is the needed increment of samples in the faster medium is quantified by the ratio between the propagation velocities in the faster and in the lower medium.

After doing this, on the other hand, the columns of the resulting matrix will be not composed by the same number of cells, just because the maximum depth reached at each abscissa is not the same. Therefore, a zero padding at the bottom of the columns is required so that at any abscissa, the spatial bottom scale becomes formally the same. After this zero padding, the combined time–depth conversion is completed, and the result is represented with depth scale ranging from zero to the maximum depth value calculated before.

Let us explicitly note that, with reference to Figure 1, the bound at which the propagation velocity should be changed is the real interface I between the two layers and not the mathematical lower interface I_1 that was introduced to perform the combined migration in the abscissa–time domain. In fact, the time–depth conversion has to be done according to the actual propagation velocities of the layers and not according to the values providing the best focalization, which in inhomogeneous media are not the same.

In Figure 2, a flow diagram of the procedure is proposed.

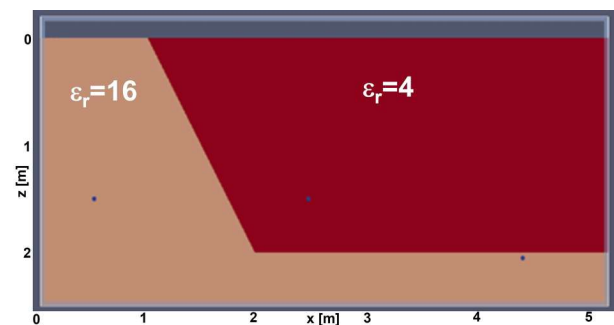


FIGURE 3 Simulated ground truth. The propagation velocity is equal to 7.5 cm/ns for the lower layer (beige) and is equal to 15 cm/ns for the upper one (purple). Please note that the measurement line does not start exactly from the bounds of the geometric domain because it is not recommended in relationship to the radiation boundary condition.

EXAMPLES

This section aims at testing the proposed strategy against numerical data generated by simulating four different scenarios reproducing realistic situations. Synthetic data have been simulated by means of the 2D version of the open-source code GPRMax (Warren et al., 2016), which is based on the finite differences in time domain numerical method. The data processing has been performed with the commercial Reflexw code (<https://www.sandmeier-geo.de/reflexw.html>, last consultation on November 22th, 2022). The combination of the

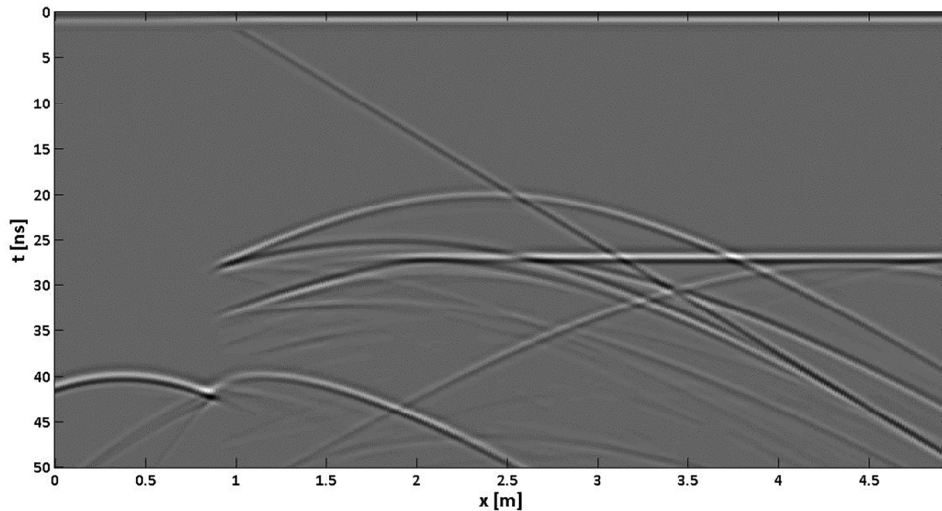


FIGURE 4 Pre-processed (non-migrated) data.

migration results and the combined time–depth conversions have been implemented through home-made codes developed in a MATLAB environment.

Two layers with the lower one somewhere emerging

The first example regards the ground truth represented in Figure 3. In particular, we have a two-layered soil and three targets embedded in it. The lower layer emerges up to the surface on the left-hand side of the figure, and in this area, there is one target. Moving from left- to right-hand, the second (central) target is in the ‘upper’ medium but at the same depth of the first target, whereas the third one is in the lower layer at a deeper level than the other two targets. All targets are perfect electric conductor (PEC) cylinders whose radius is 2 cm. The target centres are at the coordinates (0.5, 1.5), (2.5, 1.5) and (4.5, 2.05), in metres. The relative permittivity of the upper layer is equal to 4, whereas that of the lower one is equal to 16. The media are lossless. Synthetic data have been generated by using a filamentary current radiating a Ricker pulse with central frequency at 600 MHz as primary source and by collecting the backscattered field with a uniform spatial offset of 1.6 cm along a measurement line whose length is 4.944 m. The measurement line is 1 cm above the air–soil interface.

Figure 4 shows the pre-processed data. In particular, we have cleaned the data with a zero timing of 2.15 ns, a background removal on the first 5 ns, and some gain increasing with the depth. The data are noiseless. Our analysis starts heuristically from Figure 4, from which we clearly distinguish and deduce an interface between the two layers, as well as the diffraction curves relative to three targets.

The diffraction hyperbolas clearly show that the propagation velocity of the waves is different in the two layers. Specifically, in the case at hand, both layers emerge, and so the diffraction hyperbolas relative to the targets centred at (0.5, 1.5) and (2.5, 1.5) provide a good evaluation of the propagation velocity exploitable for both the separate focalization and time–depth conversion. Note that the estimated wave propagation velocity values are 15 cm/ns (this means a relative permittivity = 4) and 7.5 cm/ns (relative permittivity = 16), respectively, for the faster layer and the slower one. Moreover, the diffraction hyperbola relative to the left-hand target, that is that centred at (0.5, 1.5), is affected and deformed by the separation between the two media, whereas the diffraction hyperbola relative to the central target centred at (2.5, 1.5) is much cleaner. The right-hand target, that is that centred at (4.5, 2.05), also shows a quite clean hyperbola, even if it is made weaker by the buried interface between the two layers.

Figure 5 shows the migrated result achieved by using a propagation velocity equal to 15 cm/ns. This result makes evident that the adopted velocity allows a good focalization of the second (middle) target, whereas it produces the so-called smile effect with regard to the first (left-hand) target. Vice versa, as can be appreciated from Figure 6, a propagation velocity equal to 7.5 cm/ns provides a good focalization of the first (left-hand) target but it provides a sort of sadness effect for the second (middle) target. The combined migration, obtained by joining the results of Figures 5 and 6, is shown in Figure 7. The separation line I_1 adopted for the combined migration is the dashed yellow line in Figure 7. Such a line goes lower than the deeper level of the interface in order to include the third (right-hand) target, which is well focused by using the propagation velocity of the upper layer, because it is quite close to the interface between the layers. As said, the

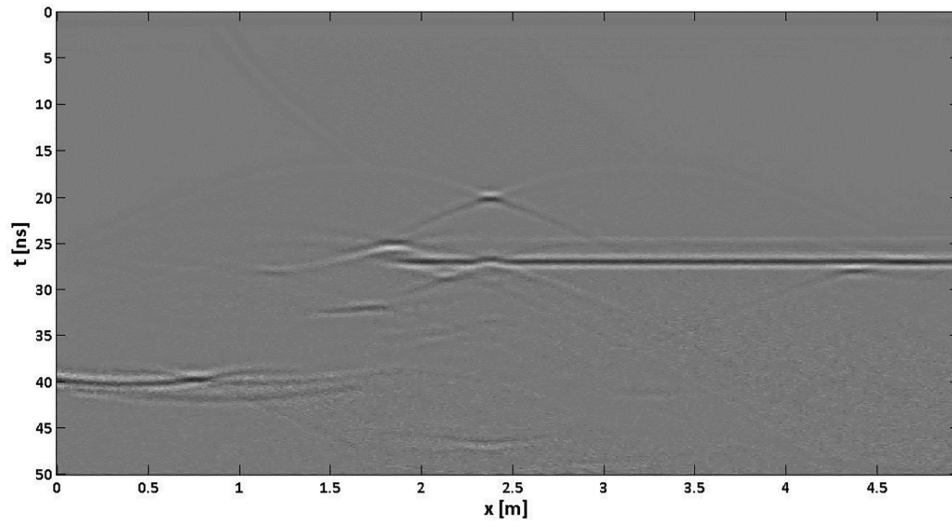


FIGURE 5 Migration of the data of Figure 3 with propagation velocity 15 cm/ns (relative permittivity = 4).

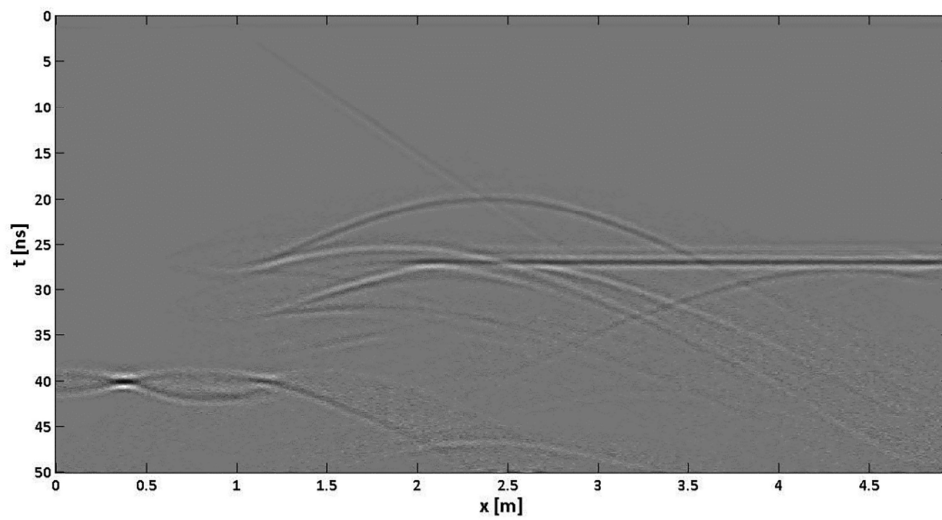


FIGURE 6 Migration of the data of Figure 3 with propagation velocity 7.5 cm/ns (relative permittivity = 16).

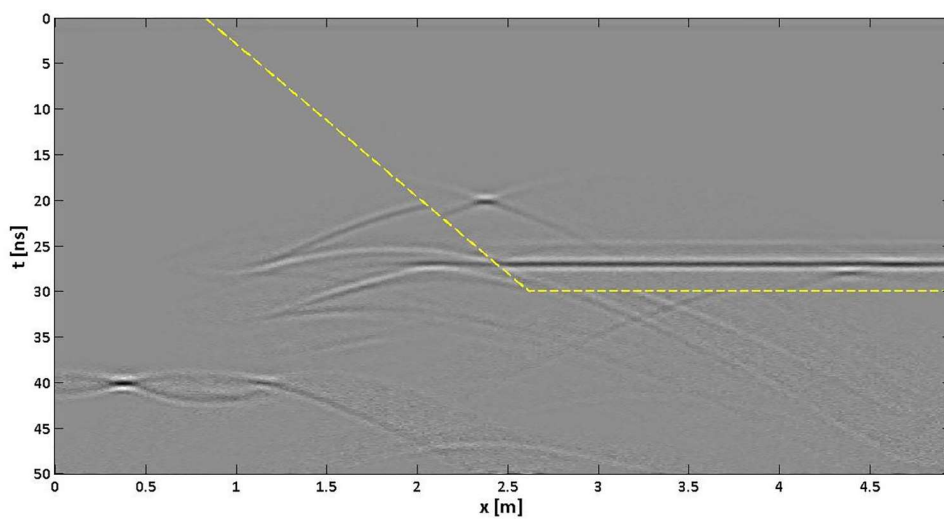


FIGURE 7 Combined migration achieved from Figures 5 and 6.

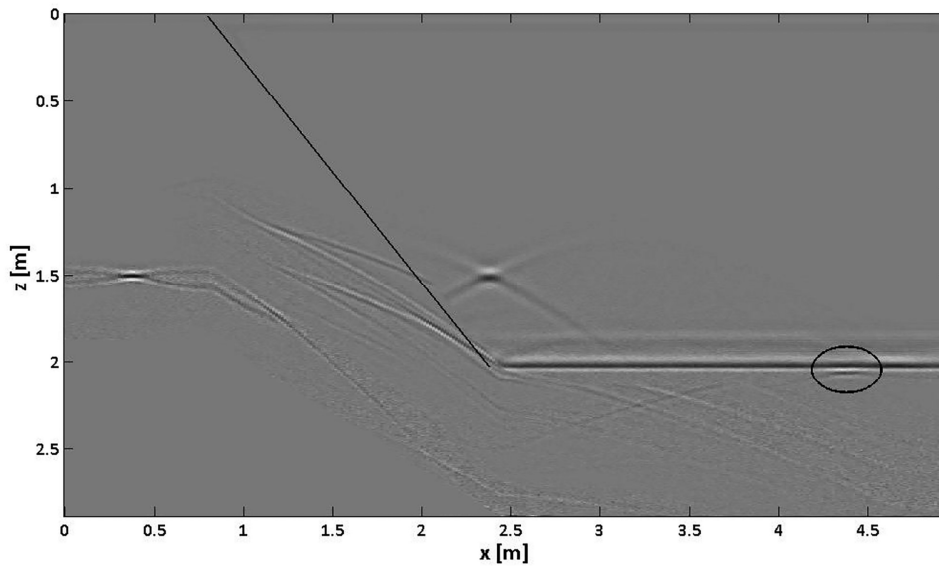


FIGURE 8 Combined time–depth conversion of the result of Figure 7.

separation line I_1 is data driven, and there is no a priori mathematical rule to determine it. Figure 7 shows that all the three targets are well focused, even if the right-hand one appears quite weak and masked by the close interface. On the other hand, we do not have ‘doubts’ about its existence because it appears in a clear way within the pre-migrated data in Figure 4 and also in Figure 6.

Figure 8 shows the combined migration result after a combined time–depth conversion. As it can be seen, the depths of the first two targets appear to be the same as it actually is, whereas this does not appear in Figures 5–7. The target on the right-hand side is put into evidence by an ellipsis. Some zero-padding effect is also visible on the left-hand side of the image. It is also evident some different qualities of the focalization, related to the different wavelengths in the two layers.

In Figure 8, the slanted part of the interface between the two layers has been depicted with an oblique straight line. Indeed, we have deduced the abscissas of the starting and end points from Figure 4, because the flat part of the buried interface is well visible also in the migrated data. It is intuitive, and it has been confirmed by several further simulations (herein not shown for sake of brevity) that the interpretation of the results becomes more difficult when the interface between the buried layers becomes strongly slanted. It is worth noting that, in the case at hand, the position of the targets with respect to the interface between the two layers is not very clear from Figure 4. This happens because the image in time domain with two different velocities makes tricky the interpretation of the positions of the targets. The focusing operated through the migration algorithm makes clearer this position, even if at the cost of making quite weaker the slanted part of the buried interface.

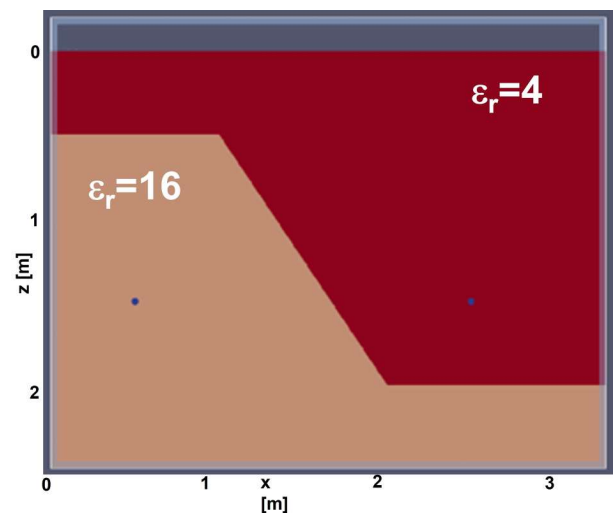


FIGURE 9 Simulated ground truth: two-layered media, the lower one everywhere covered by the upper one.

Two layers with the lower one covered everywhere by the upper one

Let now consider a further scenario made of a two-layered soil. Now, the lower layer does not emerge in any point, so the scenario at hand is formally analogous to that sketched in Figure 1. This case is trickier than the previous one because, as said, the ground-penetrating radar (GPR) data do not easily reveal the propagation velocity in the lower medium. The media have the same characteristics of the previous example, namely the relative permittivity is 4 for upper layer (propagation velocity of the waves equal to 15 cm/ns) and 16 for the lower one (propagation velocity equal to 7.5 cm/ns). The measurement configuration is the same as in the

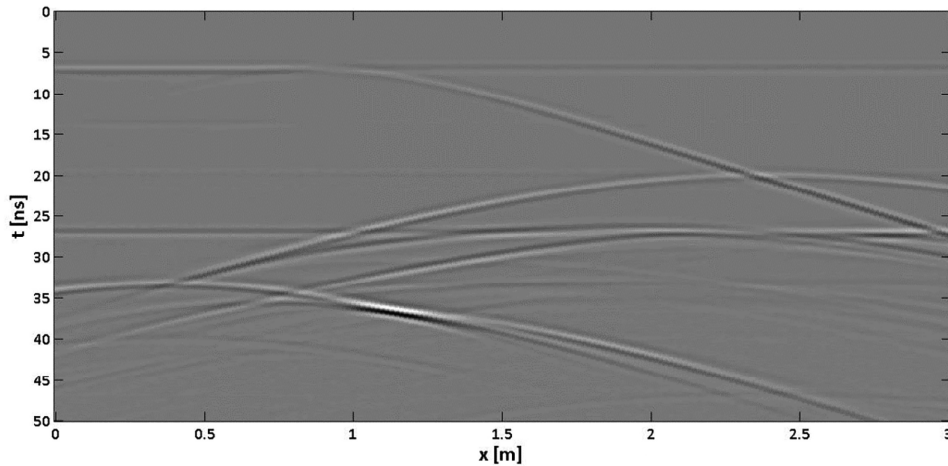


FIGURE 10 Pre-processed (non-migrated) data with the ground truth of Figure 8.

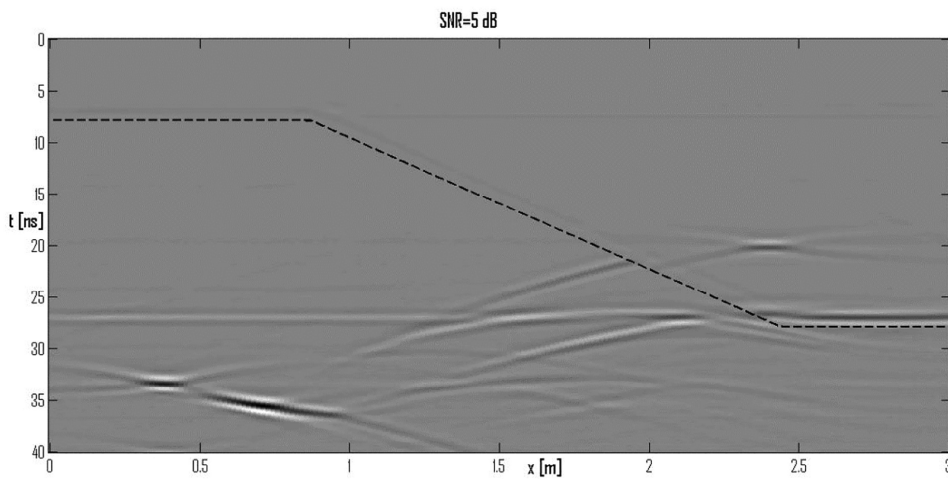


FIGURE 11 Result achieved from a joint migration (propagation velocity equal to 15 cm/ns for the upper layer and 10 cm/ns for the lower one).

previous example. The observation line is long 3 m, and the targets are two PEC cylinders, whose centres are at (0.5, 1.5) and (2.5, 1.5) m. This time, a white Gaussian noise (signal to noise ratio [SNR] = 5 dB) corrupts the simulated data, and this allows us to show that the results are quite robust with respect to the noise. The scenario is depicted in Figure 9, whereas, in Figure 10, the pre-processed (but non-migrated) data are shown, analogously to Figure 4. For brevity, this time we avoid showing the separated migration results and present directly the result of the combined migration in Figure 11 and the result of the combined time–depth conversion in Figure 12. It is worth noting that the best focusing of the target in the lower medium has been achieved with a propagation velocity of 10 cm/ns (i.e. a relative permittivity equal to 9). So, as heuristically preconized, the best focusing in the lower medium, as suggested by the diffraction curves, is not achieved inserting the correct propagation velocity in the migration algorithm. For a correct combined

time–depth conversion, however, we will use in any case the correct propagation velocity in the lower medium that here is supposed retrieved from other measurements (carrots, local ground truthing, time domain reflectometry and so on). In the example at hand, no target is seen close to the buried interface, and so in this case, we have chosen the interface for the combined migration (I_1) and that for the combined time–depth conversion (I) coinciding.

As Figure 12 shows, thanks to the combined migration and the combined time–depth conversion, both targets are focused and located at the same depth as they are, whereas this does not appear in Figure 10.

Empty cavities

Let us consider the case of two buried cavities, whose top and bottom are both visible in the data. In real cases, this

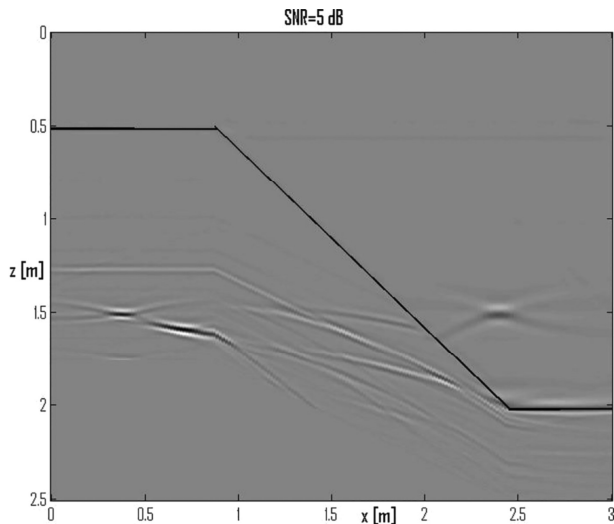


FIGURE 12 Result achieved from a combined time–depth conversion (propagation velocity equal to 15 cm/ns for the upper layer and 7.5 cm/ns for the lower one).

sometimes happens (Persico et al., 2014, 2019) and sometimes does not (Matera et al., 2016). Moreover, not always we can be sure that a certain anomaly is a cavity, but often the GPR data (and the context) allow the correct interpretation of cavities larger than the probing wavelength. In the example at hand, the left-hand cavity is sized $80 \times 65 \text{ cm}^2$, and its upper left vertex is at (0.25, 0.05) m; the right-hand cavity is sized $50 \times 70 \text{ cm}^2$, and its upper left vertex is at (2.05, 0.3) m. In the simulated scenario, also two PEC cylinders are present. Their radius is equal to 2 cm, and they are centred at (1.55, 0.45) and (2.83, 0.8) m, respectively. All the objects are embedded in a lossless medium having relative permittivity equal to 16 (corresponding to a propagation velocity of 7.5 cm/ns). The measurement configuration is the same as in the previous examples. This means, in particular, that the central wavelength in the soil is 12.5 cm, and so the cavities are not electrically small.

The observation line is 3 m long, and a Gaussian white noise is added to the data (SNR = 20 dB). According to the diffraction hyperbolas referred to the small targets, the estimated propagation velocity of the embedding medium is 7.7 cm/ns, and such a value is exploited for the data migration.

In the case at hand, each cavity behaves locally as a three-layered medium composed (from the top to the bottom) of the embedding medium, the void space and, again, the embedding medium. Here, we consider the time–depth conversion problem starting from the result of a migration performed with the estimated permittivity of the embedding medium.

In Figure 13, the scenario is depicted, whereas, in Figure 14, the result of the Kirchhoff migration (after some straightforward pre-processing) is shown. As expected, the small targets are well focused, whereas the cavities appear compressed as often happens in practice (Persico et al., 2014).

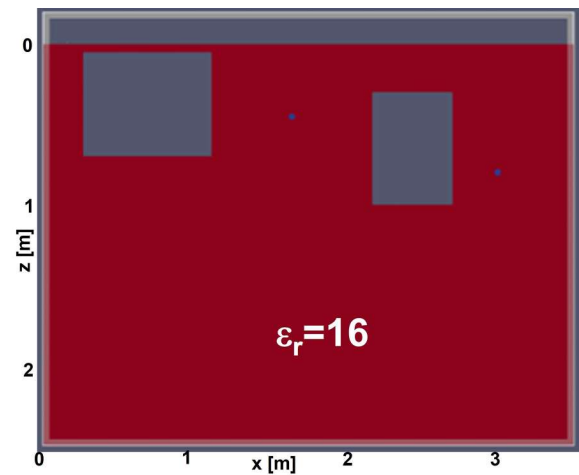


FIGURE 13 Simulated ground truth: two cavities and two small targets into a homogeneous medium.

Moreover, the shallower cavity gives an answer substantially different with respect to the deeper one.

In order to apply a combined time–depth conversion, we have to deduce from the data the starting and the ending abscissas of the cavities. We have done this by accounting for the top of the cavities that, as expectable, is more clearly visible than the bottom. Based on Figure 14, we have deduced that the first (left-hand) cavity starts at the abscissa 15 cm and ends at the abscissa 90 cm, whereas its time–depth range starts from 1.62 ns and extends up to 5.33 ns. The second (right-hand) cavity starts from 1.95 m and extends up to 2.42 m along the abscissa, whereas its time–depth extension ranges from 8 up to 12.8 ns. In order to make more realistic this deduction, two different people have simulated the data and deduced the size of the cavities, the second of which ignoring the data of the input geometry. On this basis, in Figure 15, we show a combined time–depth conversion, where the propagation velocity estimated for the embedding medium has been exploited before and after the cavities along the time axis, whereas within the cavities, we have imposed the propagation velocity of the electromagnetic waves in free space.

The algorithm for the combined time–depth applied in this section is an extension of that applied for a two-layered medium, because it accounts for three local layers (the upper and the lower one showing the characteristics of the embedding medium and the central one made of free space) instead of two. However, the approach is conceptually similar to the previous case, and its implementation is straightforwardly deduced from the previous case. Of course, to apply the time–depth conversion means that we infer from the data and/or from some a priori information that the large targets seen in the radargram are empty cavities, and so the achievable improvement is conditionally valid, as far as this assumption is correct. As Figure 15 shows, the properly time–depth converted image reproduces the thickness of the cavities in

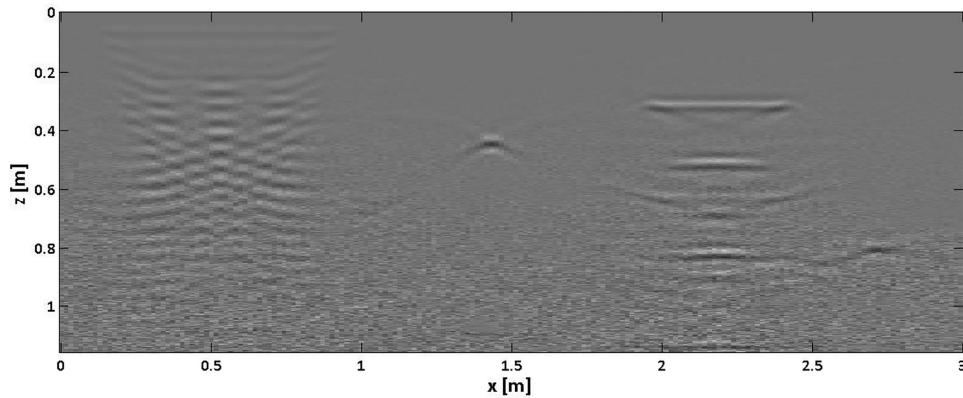


FIGURE 14 Result of a Kirchhoff migration with $v = 7.7$ cm/ns.

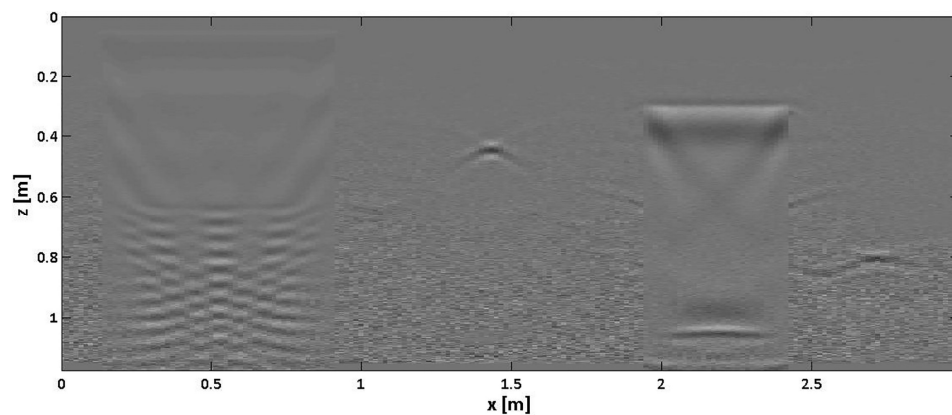


FIGURE 15 Result of a combined time–depth conversion for the result of Figure 14.

a better way and it makes correctly perceivable the relative positions of the cylinders with respect to the cavities.

A case with meaningful topography of the air soil interface

The last considered scenario regards a soil with a meaningful topography. The ground truth is represented in Figure 16. In this case, the air soil interface follows a circular shape (we have chosen a circumference with radius 2 m), and the wave propagation velocity of the soil is 7.5 cm/ns, corresponding to a relative permittivity equal to 16. The targets are three small PEC cylinders having radius 0.02 m long and centres at 0.3, 1.65, 2.7 m along x , and at 0.225, 0.50 and 0.202 m depth, respectively. The depth of each target is taken from the point at the interface placed along the vertical direction starting from the buried cylinder. The measurement line is curved and follows the air–soil interface. When representing the raw data, they appear as gathered along a flat line. However, in the most common codes for GPR data processing, there are tools for the topographic correction. In the case at hand,

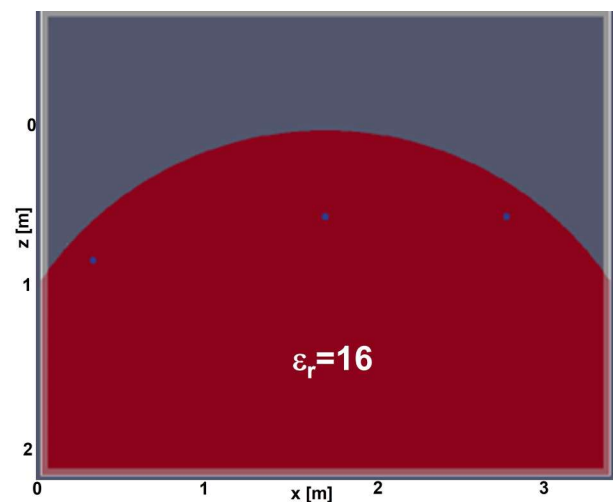


FIGURE 16 Simulated ground truth in a case with a curved interface.

the measurement configuration is still the same of the previous cases but for the curvature of the observation line. The observation line is 2.71 m long, and the spatial step of the data

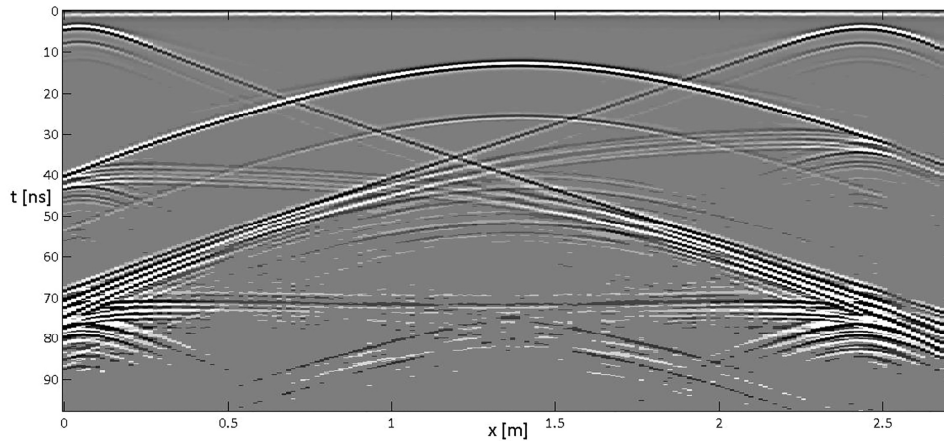


FIGURE 17 Pre-processed (non-migrated) data with the ground truth of Figure 15.

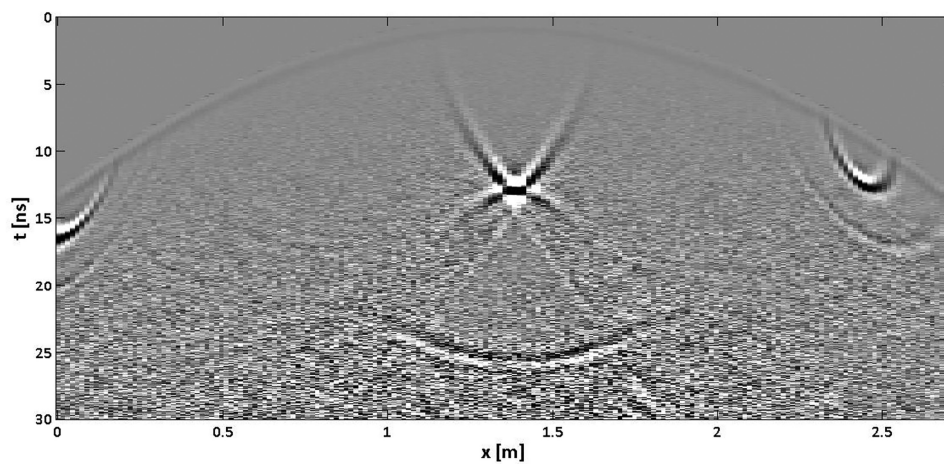


FIGURE 18 Data migrated with $v = 8.3$ cm/ns and topographic correction in time domain performed according to the actual propagation velocity equal to 7.5 cm/ns.

is 1.456 cm, whereas the time bottom scale is 100 ns. The data are also corrupted by Gaussian noise with $\text{SNR} = 20$ dB.

In Figure 17, the pre-migrated data are shown, before the topographic correction (just a zero-time correction and some gain vs. depth has been applied). In Figure 18, the migrated and topographically corrected data are shown. The migration has been performed with a propagation velocity of 8.3 cm/ns, which allows the best focusing of the central target (the other ones are peripheral, and it is physically impossible to achieve a good focalization for them (Persico et al., 2017)). In Figure 18, the time axis has been cut to the range of interest that is from 0 to 30 ns. Instead, the topographic correction (in time domain) has been implemented converting the difference of height levels of the interface in time discrepancies according to the correct propagation velocity in the soil. In this way, applying the time–depth conversion with this velocity, the spatial differences of height will come back to their actual (measured) values, and the buried targets will be placed auto-

matically at their correct depth level. Indeed, no combined time–depth conversion is needed in this case. However, also in this case, the correct propagation velocity is not deduced from the diffraction curves, because they are distorted by the curvature of the air–soil interface. Rather, they are achieved by means of other methods as listed in ‘Two layers with the lower one covered everywhere by the upper one’ section. Figure 19 shows the time–depth conversion of the data in Figure 18. For comparison, Figure 20 shows the result achieved by migrating the data with the exact value of the propagation velocity. As it can be seen, the central target now is not well focused.

EXPERIMENTAL RESULTS

In order to perform an experimental validation, we have implemented a set-up built as follows. A wooden box sized 100×50 cm and high 50 cm has been assembled. It has been

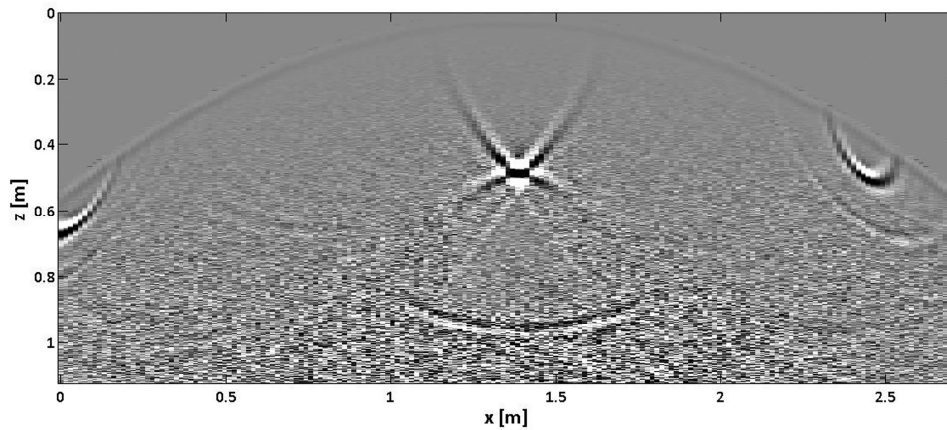


FIGURE 19 Time–depth conversion of the migrated and topographically corrected data of Figure 17.

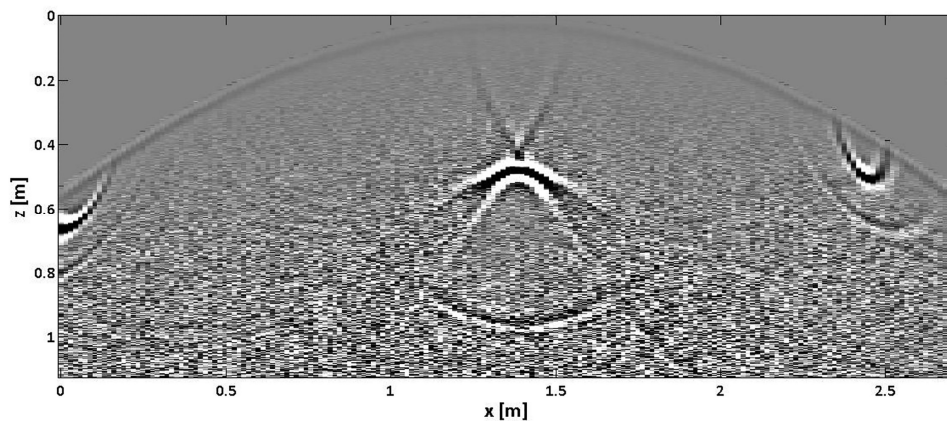


FIGURE 20 Data migrated, topographically corrected and time–depth converted according to the correct value of the propagation velocity.

filled with a terrain up to about 15 cm from its bottom. At this level, a metallic rod has been displaced as shown in Figure 21 panel A. Then the box has been further on filled with soil up to the level of 25 cm from the bottom. At this point, a thin wooden panel has been posed, and a second metallic rod has been posed as shown in Figure 21 panel B. The upper layer so created has been filled up with sand up to the edge as shown in Figure 21 panels B and C. Finally, a further thin wooden panel has been put on the top in order to avoid problems with the metric wheel of the ground-penetrating radar (GPR) system.

We have then gathered GPR data along parallel lines long about 1 m (indeed slightly less because of the size of the antenna), with interline distance of 2 cm. Here, the processed central B-scan is shown. The exploited GPR system has been a Ris Hi-Mode pulsed GPR equipped with an antenna at nominal central frequency of 2 GHz. The in-line spatial step of the data was 1 cm, whereas the time step was 0.0625 ns. The initial time bottom scale was 64 ns, but the data have been cut up to the time depth of 20 ns, because the bottom of the box corresponded to a return time of about 16.6 ns.

As described, in the end, we have two rods embedded in a two-layered medium. The shallower rod is at a depth of about 24.5 cm calculating also the radius of the rod and is at the bottom of the upper layer. The deeper rod is at the depth of about 35 cm and is embedded of course in the second layer. From preliminary measurements, performed before filling up also the sand layer, we have evaluated a propagation velocity of 6 cm/ns, corresponding to a relative permittivity of the terrain equal to 25. It is a quite high value but unfortunately the terrain was clay-like and contained very high percentage of moisture, because of the rains occurred. This made it also difficult to displace this terrain in the box without small voids that could not be completely avoided. Instead, the sand was purchased and was much drier and definitely more homogeneous. From the diffraction hyperbola of the shallower rod, we have evaluated in the sand a propagation velocity of 12 cm/ns, corresponding to a relative permittivity equal to 6.25.

Before the migration, the data have been pre-processed with a zero timing at 4.07 ns, a background removal a time cut at 20 ns, some gain versus depth linear and exponential

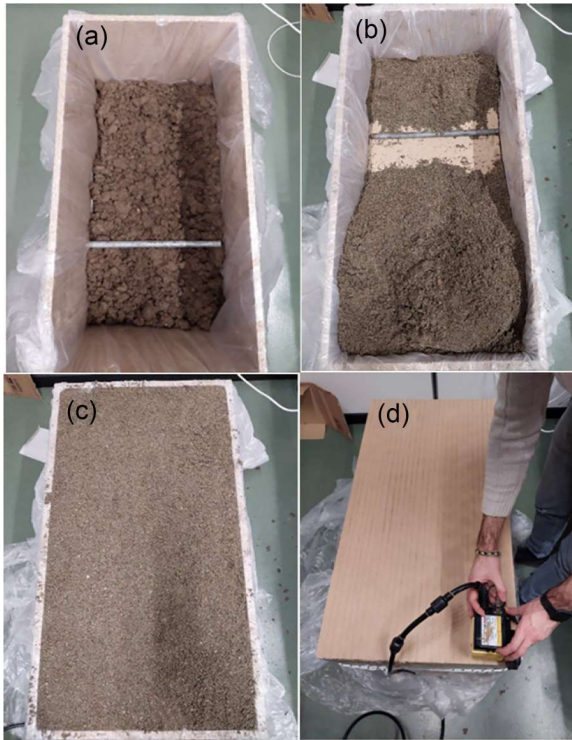


FIGURE 21 Subsequent phases of the preparation of the experimental set-up. Panel a: metallic rod displaced in wet claly soil at 15 cm from the bottom. Panel b: separation wooden sheet at 25 cm from the bottom and second metallic rod displaced on it. Panel c: upper part of the tank filled with sand. Panel d: the tank covered with a further wooden sheet and with the antenna gathering the data.

and finally a Butterworth filtering of each trace in the band 400–4000 MHz. The gain has been applied starting from the time depth of 5 ns, in order not to saturate the depth levels before the interface between the two layers. Then, we have performed two migrations, the first one making use of a propagation velocity of 12 cm/ns and the second one making use a propagation velocity of 11 cm/ns (in both cases, 81 traces have been integrated in the migration procedure). In particular, 12 cm/ns is the propagation velocity of the waves in the upper layer, whereas 11 cm/ns is the value that heuristically provided the best focalization of the rod embedded in the deeper layer. As can be seen, this value is quite different from the actual value of the propagation velocity of the waves in the deeper layer that as said is equal to about 6 cm/ns. In Figure 22, the result of a migration with velocity of 12 cm/ns is shown, whereas, in Figure 23, the homologous result with velocity of 11 cm/ns is shown.

As can be seen, the rod in the upper medium (abscissa about 0.65 m and depth time about 4.4 ns) is better focused with propagation velocity 12 cm/ns, whereas the rod in the lower layer (abscissa about 0.25 m and depth time about 7 ns) is better focused with propagation velocity equal to 11 cm/ns. Indeed, we note a strong worsening of the focalization of

the shallower rod migrating with the velocity of 11 cm/ns, whereas we note only a slight (but perceivable) worsening when the deeper rod is focused with a velocity of 12 cm/ns. Moreover, the deeper rod appears almost double: This is due to the fact that the lower embedding medium was not homogeneous as said, and the targets are visible less clearly than in the upper layer. The combined migration is shown in Figure 24, as can be seen both rods are focused at best in this image. In order to join the migration results of Figures 22 and 24, a transition between the two images has been imposed in the time–depth range 4.6–5.6 ns, that is at the interface between the two layers. The graduality of the joining (Persico & Morelli, 2020, 2021) prevents from seam effects between the two pieces of reconstruction. Finally in Figure 25, the combined migration of Figure 24 has been time–depth converted, according to the propagation velocities 12 and 6 cm/ns, with a transition at the interface between the two layers (in this examples the two lines I and I₁ schematized in Figure 1 coincide, because we do not have boundary targets in the second medium to focus properly). Figure 25 has been cut at the depth of 0.5 m, that is the thickness of the box. As can be seen, the two rods appear quite close to their nominal depth levels and, of course, also their abscissas are well imaged. To this pros, please note that the B-scan is slightly short than the length of the box (91 cm against 100 cm) due to the size of the antenna, that is of the order of 10 cm as can be appreciated from Figure 21 panel D. Finally, it can be noted a different resolution in the two layers, that is due to the different central wavelengths.

CONCLUSIONS

This paper has tackled non-canonical situations, that is scenarios where the assumptions implicitly done in widespread ground-penetrating radar data processing tools are not valid. Virtual data have been generated by means of the 2D version of the open-source code GPRMax and have been processed starting from the hypothesis that no more refined mathematical tools than those available in a commercial data processing code are available. Moreover, an experimental test has been executed.

The aim has been to exploit, in the best way, imaging algorithms based on models that we a priori know to be not correct. In other words, the effort here has been to exploit in the best way mathematically imperfect (but commonly available) processing tools. This has brought to observe that the wave propagation velocity driving to the best focusing is not in general the actual velocity value, even if this latter is in any case the value allowing the correct (combined) time–depth conversion. In this frame, a combined migration and/or a combined time–depth conversion accounting for the inhomogeneity of the host medium have been proposed in four simulated

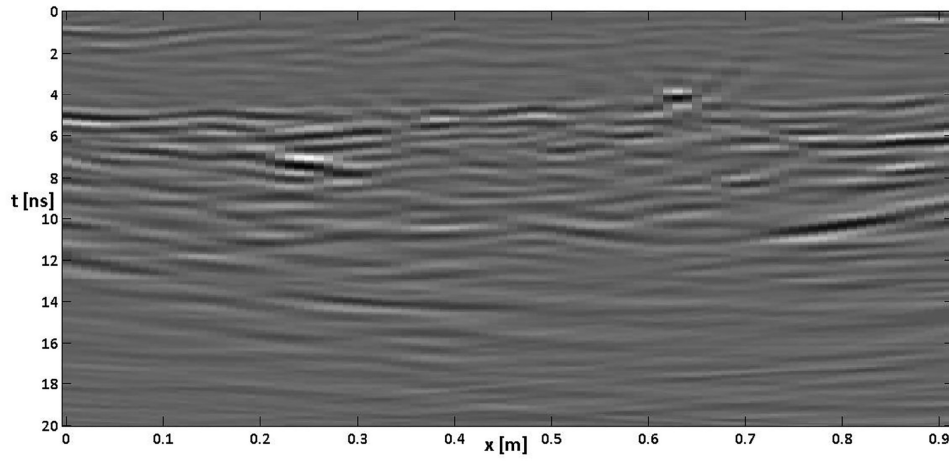


FIGURE 22 Result of a migration with propagation velocity equal to 12 cm/ns.

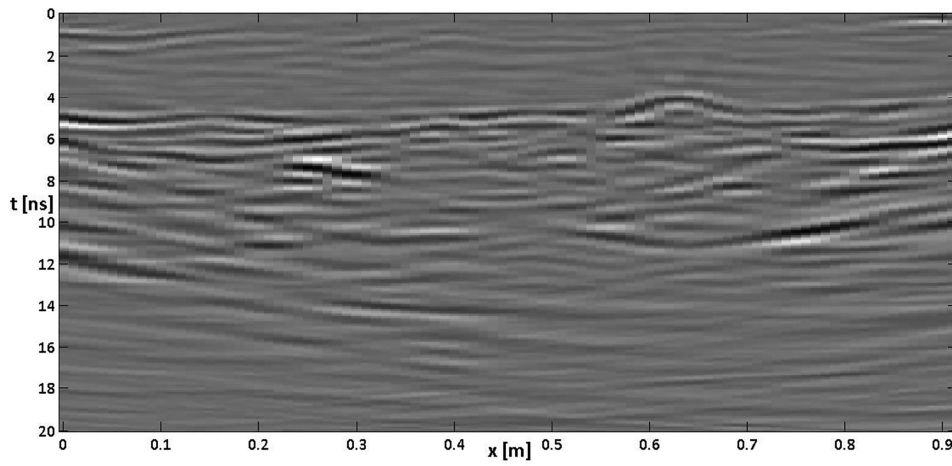


FIGURE 23 Result of a migration with propagation velocity equal to 11 cm/ns.

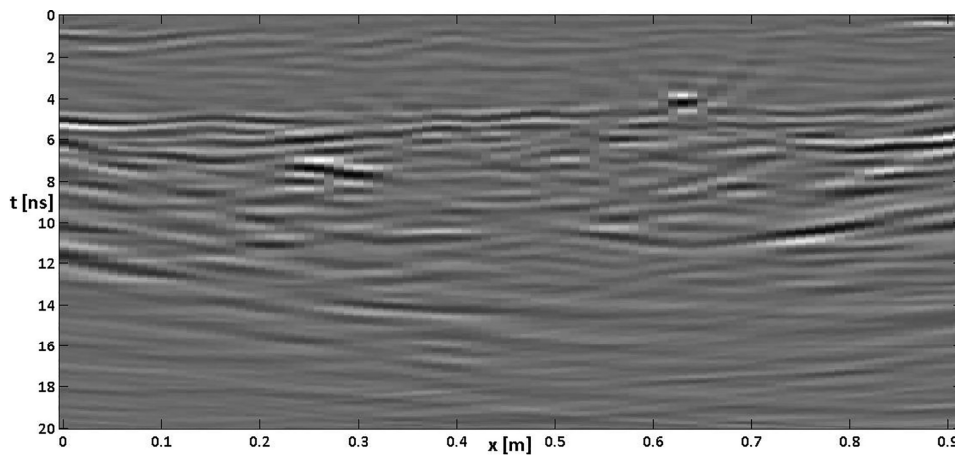


FIGURE 24 Result of the combined migration.

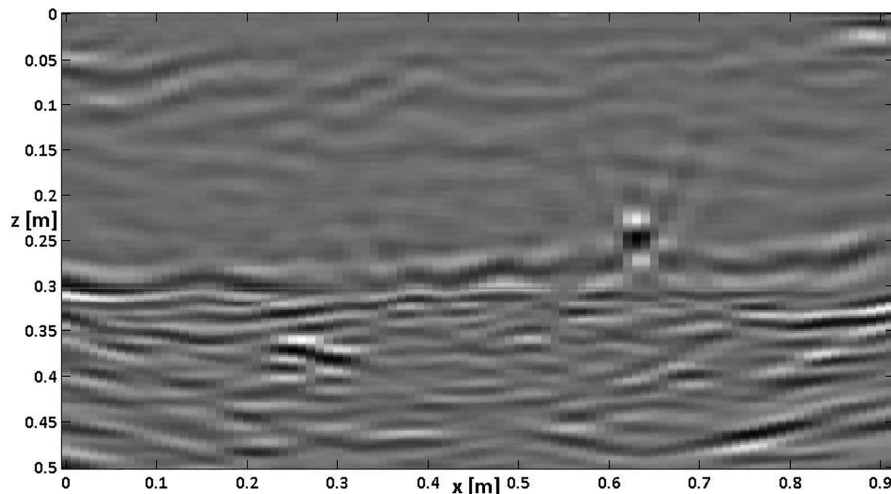


FIGURE 25 Result of the combined migration and time–depth conversion.

scenarios, and a test case with a two-layered media has been also implemented.

Combined time–depth conversions assume a particular relevance if depth slices have to be calculated in situations analogous to those described in the presented examples. In fact, in such a case, time-slices are evidently affected by the local stratification or by the topography. In these cases, slices retrieved directly in space domain after combined conversion can be more reliable.


As a last consideration, the proposed method could also be exploited in combination with algorithms based on more correct models (Alani et al., 2020; Chew, 1995; Feng et al., 2022; Mao et al., 2021; Moghaddam et al., 2005; Wang et al., 2019; Ye & Chen, 2017), within an iterative procedure. In particular, if strong discontinuities of the dielectric permittivity are present in the scenario, these could make problematic the automatic convergence of an iterative procedure starting from a homogeneous model of the soil. In these cases, if a ‘human intervention’ performed by means of a combined migration and time–depth conversion is reasonable (which can be deemed from the context and on the basis of the first achieved results), it is possible to achieve a starting scenario closer to the ground truth.

As a future development, our purpose is to implement user friendly codes for the combined migration and the combined time–depth conversion. These codes shall exploit computer graphic tools, enabling the user to draw buried interfaces as deduced (if deducible) from the data, easily and in real time.

DATA AVAILABILITY STATEMENT

The data that support the findings of this study are available from the corresponding author upon request.

ORCID

Raffaële Persico  <https://orcid.org/0000-0003-3213-2879>

REFERENCES

- Alani, A.M., Giannakis, I., Zou, L., Lantini, L. & Tosti, F. (2020) Reverse-time migration for evaluating the internal structure of tree-trunks using ground-penetrating radar. *NDT & E International*, 115(10), 102294.
- Cataldo, A., De Benedetto, E. & Cannazza, G. (2011) *Broadband reflectometry for enhanced diagnostics and monitoring applications*. Berlin, Germany: Springer-Verlag.
- Catapano, I., Gennarelli, G., Ludeno, G., Persico, R., Soldovieri, F. (2019) Ground-penetrating radar: operation principle and data. In: *Wiley encyclopedia of electrical and electronics engineering*. Wiley. <https://doi.org/10.1002/047134608X.W8383>.
- Chew, W.C. (1995) *Waves and fields in inhomogeneous media*. Hoboken, NJ: Wiley-IEEE Press.
- Colica, E., Antonazzo, A., Auriemma, R., Coluccia, L., Catapano, I., Ludeno, G. et al. (2021) GPR investigation at the archaeological site of Le Cesine, Lecce, Italy. *Information*, 12(10), 412. <https://doi.org/10.3390/info12100412>.
- Conyers, L. & Goodman, D. (1997) *Ground-penetrating radar: an introduction for archaeologists*. Lanham, MD: AltaMira Press.
- Feng, D., Li, T., Li, G. & Wang, X. (2022) Reverse time migration of GPR data based on accurate velocity estimation and artifacts removal using total variation de-noising. *Journal of Applied Geophysics*, 198, 104563.
- Gennarelli, G., Catapano, I., Dérobert, X. & Soldovieri, F. (2021) A ground penetrating radar imaging approach for a heterogeneous subsoil with a vertical permittivity gradient. *IEEE Transactions on Geoscience and Remote Sensing*, 59(7), 5698–5710. <https://doi.org/10.1109/TGRS.2020.3024831>.
- Lambot, S. & André, F. (2014) Full-wave modeling of near-field radar data for planar layered media reconstruction. *IEEE Transactions on Geoscience and Remote Sensing*, 52(5), 2295–2303. <https://doi.org/10.1109/TGRS.2013.2259243>.
- Mao, X., Zhou, Y., Lei, F., Zhao, L. & Zeyde, K. (2021) Reverse-time migration by combining laplacian filtering with wavefield decomposition for high-resolution subsurface imaging. *IEEE Journal on Multiscale and Multiphysics Computational Techniques*, 6, 73–80.

- Matera, L., Persico, R., Geraldi, E., Sileo, M. & Piro, S. (2016) GPR and IRT tests in two historical buildings in Gravina in Puglia, Geoscientific Instrumentation. *Methods and Data Systems*, 5, 541–550.
- Moghaddam, M., Chew, W.C. & Oristaglio, M. (2005) Comparison of the Born iterative method and Tarantola's method for an electromagnetic time-domain inverse problem. *International Journal of Imaging Systems and Technology*, 3(4), 318–333.
- Persico, R., Ciminale, M. & Matera, L. (2014) A new reconfigurable stepped frequency GPR system, possibilities and issues; applications to two different Cultural Heritage Resources. *Near Surface Geophysics*, 12(6), 793–801 <https://doi.org/10.3997/1873-0604.2014035>.
- Persico, R., D'Amico, S., Matera, L., Colica, E., De Giorgio, C., Alescio, A. et al. (2019) GPR investigations at St John's co-cathedral in Valletta. *Near Surface Geophysics*, 17(3), 213–229. <https://doi.org/10.1002/nsg.12046>.
- Persico, R., Leucci, G., Matera, L., de Giorgi, L., Soldovieri, F., Cataldo, A. et al. (2015) Effect of the height of the observation line on the diffraction curve in GPR prospecting. *Near Surface Geophysics*, 13(3), 243–252.
- Persico, R., Ludeno, G., Soldovieri, F., De Coster, A. & Lambot, S. (2017) 2D linear inversion of GPR data with a shifting zoom along the observation line. *Remote Sensing*, 9, 980. <https://doi.org/10.3390/rs9100980>. Open access.
- Persico, R. & Morelli, G. (2020) Combined migrations and time-depth conversions in GPR prospecting: application to reinforced concrete. *Remote Sensing*, 12(17), 2778. Open access. <https://doi.org/10.3390/rs12172778>.
- Persico, R. & Morelli, G. (2021) Combined migration results and time-depth conversions in two layered media. In: Proc. of 11th International Workshop on Advanced Ground Penetrating Radar IWAGPR, Valletta, Malta, December 1–4, 2021.
- Schneider, W.A. (1978) Integral formulation for migration in two and three dimensions. *Geophysics*, 43(1), 49–76.
- Stolt, R.H. (1978) Migration by Fourier transform. *Geophysics*, 43(1), 23–48.
- Warren, C., Giannopoulos, A. & Giannakis, I. (2016) gprMax: open source software to simulate electromagnetic wave propagation for ground penetrating radar. *Computer Physics Communications*, 202, 163–170.
- Webster, J.G., Catapano, I., Gennarelli, G., Ludeno, G., Soldovieri, F. & Persico, R. (2019) Ground-penetrating radar: operation principle and data processing. In: Webster, J.G. (Ed.) *Wiley encyclopedia of electrical and electronics engineering*. <https://doi.org/10.1002/047134608X.W8383>.
- Ye, X. & Chen, X. (2017) Subspace-based distorted-Born iterative method for solving inverse scattering problems. *IEEE Transactions on Antennas and Propagation*, 65(12), 7224–7232.
- Zhang, Y., Wang, L., Feng, N., Zhuang, M., Feng, X., Fang, G. et al. (2019) A 3-D high-order reverse-time migration method for high-resolution subsurface imaging with a multistation ultra-wideband radar system. *IEEE Journal of Selected Topics in Applied Earth Observations and Remote Sensing*, 12(2), 744–751.

How to cite this article: Persico, R., Marasco, F., Morelli, G. & Esposito, G., Catapano, I. (2023) A posteriori insertion of information for focusing and time–depth conversion of ground-penetrating radar data. *Geophysical Prospecting*, 71, 1756–1771. <https://doi.org/10.1111/1365-2478.13369>